

See discussions, stats, and author profiles for this publication at: <https://www.researchgate.net/publication/262340993>

# The identification of coherent structures using proper orthogonal decomposition and dynamic mode...

Article in Journal of Fluids and Structures · August 2014

DOI: 10.1016/j.jfluidstructs.2014.04.002

---

CITATIONS

14

READS

508

3 authors, including:



[Yingzheng Liu](#)

Shanghai Jiao Tong University

138 PUBLICATIONS 633 CITATIONS

[SEE PROFILE](#)

Some of the authors of this publication are also working on these related projects:



Fluid-Struture-Acoustics of Control Valves: CFD and Experiments [View project](#)

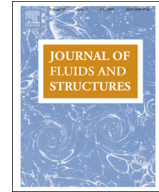


End-wall heat transfer study for bluff bodies by using temperature sensitive paint [View project](#)



Contents lists available at ScienceDirect

## Journal of Fluids and Structures

journal homepage: [www.elsevier.com/locate/jfs](http://www.elsevier.com/locate/jfs)

# The identification of coherent structures using proper orthogonal decomposition and dynamic mode decomposition

Qingshan Zhang, Yingzheng Liu\*, Shaofei Wang

*Key Lab of Education Ministry for Power Machinery and Engineering, Gas Turbine Research Institute, School of Mechanical Engineering, Shanghai Jiao Tong University, 800 Dongchuan Road, Shanghai 200240, China*

## ARTICLE INFO

### Article history:

Received 9 May 2013

Accepted 13 April 2014

### Keywords:

Vortex dynamics

Coherent structure

Proper Orthogonal Decomposition

Dynamic Mode Decomposition

## ABSTRACT

A comprehensive comparison was conducted on the identification of coherent structures in fluid flow using Proper Orthogonal Decomposition (POD) and Dynamic Mode Decomposition (DMD). The influences that multi-dominant structures and high-order harmonics had on the decomposed modes were taken into extensive consideration. To this end, a series of fabricated patterns was constructed for the benchmark testing to simulate multi-dominant convective structures superimposed in a stationary field. The comparison showed that the temporal DMD method could clearly separate each structure in the spatial and spectral senses, while the POD mode corresponding to the desired structure is contaminated by the other uncorrelated structures. Subsequently, two case studies of the real wake flows, which were determined from high-repetition TR-PIV measurements, were employed to demonstrate the discrepancies of the POD and DMD algorithms in extracting coherent structures. For the wake flow behind a single cylinder at  $Re_D = 8000$ , the temporal DMD algorithm accurately determined the frequency, wavelength and convection speed of the Karman-like vortex street and its higher-order harmonics. However, although the first two POD modes are closely related to the Karman-like vortex street, the higher POD modes embedded as larger structures are obscure in the physical significance. Finally, the wake flow behind two side-by-side cylinders of different diameters at  $Re_D = 1000$  based on the diameter of the small cylinder was measured; two configurations with different gaps were chosen for comparison, i.e.,  $G/D = 0.5$  and  $2.0$ . For the wake flow at  $G/D = 0.5$ , the POD and DMD algorithms determined the major features of the single-dominant structure. For the wake flow at  $G/D = 2.0$ , the first and second temporal DMD modes effectively and independently extracted the Karman-like vortex structures behind the large and small cylinders, respectively. Meanwhile, although the first and second pairs of POD modes generally captured these two convecting structures, respectively, there was obvious existence of the undesirable contamination of the POD mode, as reflected in the interaction between the desired and uncorrelated structures.

© 2014 Elsevier Ltd. All rights reserved.

## 1. Introduction

Fluid flows such as wakes, jets, and separated flows are largely characterized by coherent structures with different spatial and temporal scales and the common existence of multi-dominant structures in fluid flows makes identifying the spatio-temporal

\* Corresponding author.

E-mail address: [yzliu@sjtu.edu.cn](mailto:yzliu@sjtu.edu.cn) (Y. Liu).

<b>Nomenclature</b>		<i>Greek symbols</i>
$A$	matrix comprised of mode coefficients $a_i(t)$	$\bar{u}$ time-mean velocity [ $\text{m s}^{-1}$ ]
$B$	system matrix	$u'$ fluctuation velocity [ $\text{m s}^{-1}$ ]
$C$	companion matrix	$v_j$ Koopman mode
$\tilde{C}$	full companion matrix	
$D$	diameter of small cylinder [m]	
$G$	gap between two cylinders [m]	
$G_{aa}$	power spectra of coefficient $a(t)$	
$M$	finite number of POD modes	
$R$	temporal correlation matrix	
$\text{Re}_D$	Reynolds number based on diameter of small cylinder	
$S$	infinite Vandermonde matrix	$\alpha_n(t)$ growth rate factor
$\tilde{S}$	finite Vandermonde matrix	$\beta_n$ wavelength factor
$K$	Koopman operator	$\gamma_n$ velocity factor
$U$	discrete velocity matrix	$\delta$ thickness of turbulent boundary layer
$U_0$	free stream velocity [m/s]	$\Lambda$ diagonal matrix with eigenvalues
$a_i(t)$	mode coefficients of POD	$\lambda_x$ characteristic wavelength along the streamwise direction
$a_n$	constant	$\lambda_i$ eigenvalues of Koopman operator
$b_n$	constant	$\mu$ eigenvalues mapping onto the complex plane
$c_i$	$c = (c_1, \dots, c_{N-1}, c_N)$	$\rho$ density of the glass beads [ $\text{kg m}^{-3}$ ]
$d$	diameter of glass beads [m]	$\sigma$ growth rate of DMD modes
$d_n$	size factor of fabricated structure	$\sigma_k(x)$ spatial eigenfunctions
$e$	$e = (0, \dots, 0, 1)^T$	$\Phi$ dynamic modes
$f$	frequency [Hz]	$  \Phi  $ energy norm of dynamic mode
$f_0$	a map comparing a manifold to itself	$\varphi_i$ Koopman eigenfunctions
$g$	vector-valued observable	$\omega$ phase velocity of DMD modes
$q$	fabricated pattern	
$q_n$	component of the fabricated pattern	
$r$	residual vector	
$T$	period of the shedding structures	
$\Delta x$	distance between two adjacent points along the streamwise direction	
$u$	instantaneous velocity [ $\text{m s}^{-1}$ ]	

<i>Abbreviations</i>	
DMD	Dynamic Mode Decomposition
DNS	Direct Numerical Simulation
LES	Large Eddy Simulation
PIV	Particle Image Velocimetry
POD	Proper Orthogonal Decomposition
RAID	Redundant Arrays of Inexpensive Disks
SSD	Solid State Disk
TR-PIV	Time-resolved Particle Image Velocimetry
WAG	Window Average Gradient

features of each coherent structure challenging. Such identification, however, plays a significant role in study of various physical processes, e.g., heat and mass transfer, and flow noise. Recent decades have seen rapid developments in remarkable applications of Large Eddy Simulation (LES) and Direct Numerical Simulation (DNS), along with the state-of-the-art Time-resolved Particle Image Velocimetry (TR-PIV) – all of which have enabled the accurate capture of instantaneously varying flows at reasonable spatial and temporal resolutions. It is highly desirable to extract the salient coherent structures from a large quantity of numerical and experimental information.

In the last two decades, many techniques have been proposed to identify the coherent structures, e.g., vorticity concentration, critical points, Window Average Gradient (WAG) detection and Q-criterion. By plotting vorticity contour maps, Hussain and Hayakawa (1987) characterized large-scale organized structures in the turbulent plane wake of a circular cylinder; the spatially phase-correlated vorticity was employed to examine the dynamics of coherent structures in turbulent shear flow (Hayakawa and Hussain, 1989) and cylinder wake (Zhou and Antonia, 1993). Using the Q-criterion, the kinematical and dynamical properties of the flow, for example kinetic energy, Reynolds stress, were made clear by describing the flows in terms of individual events or streamline patterns (Hunt et al., 1988). Bisset et al. (1990) detected the organized motion in a cylinder wake by calculating the WAG value. Zhou and Antonia (1994) applied the critical point method in analysis of a turbulent near wake, demonstrating that the spanwise vortices provide the dominant contribution to the Reynolds shear stress. The above-mentioned methods have been extensively employed in fluid-mechanics community to determine characteristics of the vortices buried in turbulent flows. However, such methods would obscure the underlying complexity of fluid flow superimposed with multi-dominant coherent structures. Among all of the data-driven algorithms that have been used to determine the spatio-temporal features of multi-scale coherent structures, Proper Orthogonal Decomposition (POD) and Dynamic Mode Decomposition (DMD) have enjoyed widespread use. A comprehensive understanding of the roles of POD and DMD algorithms in the identification of multi-dominant coherent structures in spatial and spectral domains is of essential significance.

Sirovich (1987) and Lumley (2007) confirmed that POD has been widely used for the past several decades to determine coherent structures from flow-field snapshots. Noack et al. (2003), Lumley (2007), and Liu et al. (2011b) published results showing that a POD algorithm extracts the most energetic structures, ranked by their own energy and with a hierarchy of coherent structure, by diagonalizing the temporal and spatial correlation matrix calculated from the snapshot sequences. The POD analysis of the instantaneous velocity fields of a turbulent jet in cross flow, obtained by Meyer et al. (2007) using stereoscopic PIV, showed that the wake vortices are the dominant dynamic structures responsible for the strong interaction with the jet core, whereas the jet shear-layer vortices are local and less dominant. For the flow around a NACA0015 foil, which was determined by Time Resolved Stereoscopic Particle Image Velocimetry (TR-SPIV), Prothén et al. (2014) employed POD analysis to highlight the unsteady nature of the wake using phase-averaging based on the first POD coefficients. Through 3-D POD reconstruction of flow fields obtained by tomographic PIV measurement, Deri et al. (2013) quantified the three-dimensional coherent vortex structures buried in the high-Reynolds number turbulent flow around a thin flat plate. However, recent studies have disclosed that the POD algorithm works well to extract the dominant structures, unless extracted modes are not ranked correctly in all circumstances, as suggested by Noack et al. (2003) and Kim et al. (2010), or the temporal information cannot be obtained from the two point correlation tensor, which is an average quantity included by Gilka et al. (2010) and Seena and Sung (2011).

The DMD algorithm recently developed by Schmid (2010) as the basis of a Koopman analysis of a dynamic system promoted by Mezić (2005) and Rowley et al. (2009) provides a compact and instructive manner for understanding the dynamic information of fluid flow. Compared to the POD algorithm, the DMD algorithm considers both the temporal (spectral) and spatial orthogonalities, resulting in the phase/frequency information and the corresponding coherent structures. Gilka et al. (2010) performed a DMD analysis of the wake behind an actuated bluff body, extracting the structures based on the time-averaged squared amplitudes of the normalized DMD modes, and the dominant frequencies of the actuated flow were determined for the dominant flow structures, which are sorted with respect to frequency and energy content. Pan et al. (2011) performed a DMD analysis of the Gurney flap wake flow, to capture the vortex shedding pattern behind the trailing edge and its high-order harmonics, including abundant information on aspects such as frequency, wavelength, and convection speed. Regarding the wake behind a high-speed train model, Muld et al. (2012) detected strong peaks in the normalized energy spectra of the DMD modes; the associated flow structures were then determined by reconstructing the flow field with the time-mean velocity and one of the DMD modes. Recently, while performing the DMD analysis of hairpin vortices generated by a hemisphere protuberance, Tang and Jiang (2012) clearly extracted the dominant structures in terms of both spectral and spatial aspects, and confirmed that the hairpin vortices shed from the hemisphere protuberance at a definite frequency rather than at several frequencies.

The aim of this study was to provide a comparative understanding of the POD and DMD algorithms in terms of identification of multi-dominant coherent structures and high-order harmonics buried in fluid flows. To this end, a series of fabricated patterns was used for benchmark testing and validation, constructed using different parts, e.g., the stationary field and multi-dominant structures with different spectral and spatial aspects. The results showed that each POD mode exhibits non-negligible contamination by the other uncorrelated structures while the temporal DMD analysis separately extracts the desired structure without discernible contamination. Subsequently, two real flow cases were employed to demonstrate the discrepancies of these two methods in identification of multi-dominant coherent structures, i.e., the wake flow behind a single cylinder, which contains several high-order harmonics superimposed with the dominant Karman-like vortex street in the disturbance field, and the wake flow behind two side-by-side cylinders of different sizes, which contains multi-dominant structures without high-order harmonics in the disturbance field.

## 2. Proper Orthogonal Decomposition

The POD algorithm was first proposed by Lumley (2007) to identify coherent structures in turbulent flows by extracting an orthogonal set of spatial eigenfunctions from the second-order statistics of a random field. The dominant features and events identified by POD are ranked based on energy, and the POD modes are calculated from the spatial correlation tensor, which is treated as an averaged quantity. This results in a loss of the dynamic information buried in turbulent flow, as subsequently discussed. A brief overview of the snapshot POD algorithm used in this study is given below. For detailed information regarding the fundamentals and mathematical processes, please refer to Lumley (2007) and Sirovich (1987).

The main philosophy of POD is to find the optimal representation of the field realizations, which generates a Fredholm integral equation

$$\int R(x, x')\phi(x')dx' = \lambda\phi(x). \quad (1)$$

A temporal sequence of flow fields consisting of column vectors  $u_i$ , with the discrete velocities for all cells at an instance, can be written as

$$U = [u_1, \dots, u_N]. \quad (2)$$

Applying the snapshot method suggested by Sirovich (1987), the velocity field  $u_i$  is decomposed into the time-mean and fluctuation components,

$$u(x, y, t_i) = \bar{u}(x, y) + u'(x, y, t_i), \quad (3)$$

where  $\bar{u}$  and  $u'$  represent the time-mean and fluctuation components of the velocity vectors, respectively. Introducing the snapshots of flow field into the matrix  $U$ , the following equation is established:

$$RA = \Lambda A, \quad (4)$$

where  $A$  is a matrix combined of mode coefficients  $a_i(t)$ ,  $\Lambda$  is a diagonal matrix with eigenvalues on the diagonal, and  $R$  is the temporal correlation matrix. Correspondingly, the fluctuating flow field is decomposed into a set of eigenfunctions and mode coefficients

$$u'(x, y, t_i) \approx \sum_{k=1}^M a_k(t_i) \sigma_k(x, y), \quad (5)$$

where  $\sigma_k(x)$  are the spatial eigenfunctions,  $a_k(t)$  are the mode coefficients, and  $M$  is the finite number of POD modes.

### 3. Dynamic Mode Decomposition

The DMD algorithm recently proposed and modified by Schmid and Sesterhenn (2009) is based on a variant of the Arnoldi algorithm suggested by Ruhe (1984) to compute DMD modes or approximate the Koopman modes for the velocity matrix  $U$ . Before the DMD algorithm is shown, the Koopman mode analysis is briefly addressed, having been recently introduced into fluid mechanics by Rowley et al. (2009). For detailed information regarding the fundamentals and mathematical processes of the DMD algorithm, please refer to Schmid (2010).

The Koopman method decomposes the flow field into a series of so-called Koopman modes in which each mode is characterized by a frequency and a growth rate. These modes are determined from spectral analysis of the Koopman operator and separated by the frequency corresponding to each flow behavior. In a Koopman mode analysis, a discrete dynamic system is ultimately considered by analyzing the discrete-time data

$$u_{k+1} = f(u_k), \quad (6)$$

where the function  $f$  shifts the velocity field  $u_k$  from one time step to the next. By definition, the Koopman operator ( $K$ ) is a linear operator

$$Kg(u_k) = g(f(u_k)), \quad (7)$$

where  $g$  is a scalar valued function and is also referred to as an observable associating a scalar with a flow field. To analyze the flow dynamics, the eigenfunctions and their corresponding eigenvalues are needed. Hence, let  $\lambda_j$  denote the eigenvalues and  $\varphi_j$  denote the eigenfunctions of the Koopman operator, and we get the eigendecomposition,

$$K\varphi_j(u) = \lambda_j \varphi_j(u), \quad j = 1, 2, \dots, \quad (8)$$

As described by Mezić (2005),  $g$  can be expanded in terms of the eigenfunctions of the Koopman operator as

$$g(u_1) = \sum_{j=1}^{\infty} \varphi_j(u_1) v_j, \quad (9)$$

where the eigenfunctions  $\varphi_j$ , referred to as Koopman eigenfunctions, and the corresponding vectors  $v_j$ , referred to as the Koopman modes of the function  $f$ , can be used as a basis of expansion for the observables at all temporal instances

$$g(u_{k+1}) = K^k g(u_1) = K^k \sum_{j=1}^{\infty} \varphi_j(u_1) v_j = \sum_{j=1}^{\infty} \lambda_j^k \varphi_j(u_1) v_j, \quad (10)$$

where  $\lambda_j$  are the Koopman eigenvalues characterizing the temporal behavior of the corresponding Koopman modes  $v_j$ . The real part of  $\lambda_j$  is the magnitude determining the growth rate, and its imaginary part is the phase determining the frequency. Here, the whole expression  $\varphi_j(u_1) v_j$  represents the spatial structures, corresponding to  $\sigma_i(x)$  in the POD algorithm. Therefore, the entire sequence of snapshots in Eq. (10) can be written as

$$U = \Phi S, \quad (11)$$

where

$$S = \begin{bmatrix} 1 & \lambda_1 & \lambda_1^2 & \dots \\ 1 & \lambda_2 & \lambda_2^2 & \dots \\ \vdots & \vdots & \vdots & \ddots \end{bmatrix}. \quad (12)$$

Now we turn to the DMD algorithm to calculate the Koopman modes. Given a sequence of  $n$  snapshots of the flow fields  $\{v_1, v_2, \dots, v_{N+1}\}$  consisting of the velocity matrix  $U_1^{N+1}$ , we assume a linear dynamic system  $B$ , through which each snapshot can be expressed as

$$v_{j+1} = B v_j. \quad (13)$$

The system matrix  $B$  is a high-dimensional linear system that captures the dominant features of a dynamic system; in particular, the eigenvalues of the matrix  $B$  disclose stability information, e.g., growth rate and phase velocities. As the number of snapshots increases, the  $(n+1)$ th snapshot is described using the previous snapshots based on the Arnoldi

promoted by Ruhe (1984)

$$u_{n+1} = \sum_{i=1}^n c_i u_i + r, \quad (14)$$

where  $c_i$  are unknown coefficients and  $r$  is the residual vector. Based on these unknown coefficients, the flow field can be written as

$$B\{u_1, u_2, \dots, u_N\} = \{u_2, u_3, \dots, u_{N+1}\} = \{u_2, u_3, \dots, u_N\}C + re^T, \quad (15)$$

or

$$BU_1^N = U_2^{N+1} = U_1^N C + re^T. \quad (16)$$

The matrix  $C$  is a companion type

$$C = \begin{bmatrix} 0 & 0 & \cdots & 0 & c_1 \\ 1 & 0 & \cdots & 0 & c_2 \\ 0 & 1 & \cdots & 0 & c_3 \\ \vdots & \ddots & & & \vdots \\ 0 & 0 & \cdots & 1 & c_N \end{bmatrix}, \quad (17)$$

which shifts the flow field to the one at the next time step. The matrix  $C$  is a proxy of the high-dimensional system matrix  $B$ , and captures the dominant behavior of the flow described by the system matrix  $B$ . The eigenvalues  $\lambda_j$  of the matrix  $C$ , which are regarded as the empirical Ritz values approximating the eigenvalues of the system matrix  $B$ , are approximations of the eigenvalues of the Koopman operator described by Rowley et al. (2009). These eigenvalues produce stability information about dynamic modes by mapping onto the complex plane as  $\mu = \log(\lambda)/\Delta t = \sigma + i\omega$ , in which the real part  $\sigma$  represents growth rate (grow or decay), and the imaginary part  $\omega$  contains the frequency information. As the eigenvalues of the companion matrix  $C$  are approximations to those of the Koopman operator, the eigenvectors of  $C$  are used to span the inverse of the finite Vandermonde matrix  $\tilde{S}$  described by Chen and Louck (1996). Rowley et al. (2009) mentioned that an approximation of the Koopman modes, combined with the Koopman eigenfunctions, can be calculated with  $\tilde{\Phi} = U_1^N S^{-1}$ . Unlike the POD modes ranked according to the corresponding eigenvalues, the DMD modes are ranked based on their contributions to the total energy in the flow field by using the global energy norm of each mode  $\|\Phi_i\|$ , as suggested by Rowley et al. (2009) and Bagheri (2010).

The above-mentioned procedure is for the temporal DMD analysis. As for the spatial DMD analysis, the flow fields should be reorganized to show in a snapshot sequence in space along the streamwise direction. For details regarding the spatial DMD analysis, please refer to Schmid (2010).

#### 4. Results and discussion

In this section, the fabricated patterns and two real flow cases for assessing and validating the POD and DMD algorithms in terms of identifying multi-dominant coherent structures buried in fluid flows are applied. In Section 4.1, a series of fabricated patterns is used for benchmark testing, which consists of the stationary field and three dominant structures with different spectral and spatial aspects. In Section 4.2, a case study of the real flow behind a single cylinder is analyzed, which contains several high-order harmonics superimposed with the dominant Karman-vortex street in the disturbance field. In Section 4.3, a case study of the real flow behind two side-by-side cylinders of different sizes is finally reviewed, which contains multi-dominant structures without high-order harmonics in the disturbance field.

##### 4.1. Fabricated patterns

To assess and validate the POD and DMD algorithms' ability to identify coherent structures, a series of fabricated patterns are constructed to simulate the multi-dominant structures buried in the fluid flow. Here, the method proposed by Seena and Sung (2011) is applied to construct the fabricated patterns

$$q = q_0 + q_1 + q_2 + q_3, \quad (18)$$

$$q_0(x, y, t) = \exp(-y^2/0.7), \quad (19)$$

$$q_n(x, y, t) = \alpha_n(t) \sum_{m=-\infty}^{m=\infty} (-1)^m \exp\left[-\left(\frac{(x-\beta_n m - \gamma_n t)^2}{d_n}\right) + \frac{y^2}{d_n}\right], \quad n = 1, 2, 3, \dots, \quad (20)$$

where  $d_n = a_n x + b_n$  is the diameter of the structure,  $a_n$  and  $b_n$  are the constants,  $\beta_n$  is the wavelength factor defined as the distance between two neighboring structures,  $\gamma_n$  is the convection velocity of the structure in the streamwise direction, and  $\alpha_n(t)$  is the growth or decay factor. The dominant frequencies of these three structures  $q_1$ ,  $q_2$ , and  $q_3$  are determined by  $f_n = \gamma_n/(2\beta_n)$ , i.e., 0.5 Hz, 1.64 Hz, and 4.0 Hz, respectively. The value of the coefficient  $\alpha_n(t)$  determines variations in the convecting structures; that is, at  $\alpha_n(t) = 1$  the structures are constant without growth or decay while the cases at  $\alpha_n(t) > 1$

and  $\alpha_n(t) < 1$  correspond to the growing and decaying structures, respectively. The fabricated multi-dominant structure pattern is composed of three different dynamic structures ( $n=1, 2, 3$ ), each of which evolves with a certain velocity at different frequencies. The parameters for each pattern are listed in [Table 1](#). [Fig. 1](#) shows instances of the stationary field, the three different structures, and the single- and multi-dominant structure patterns. The structures  $q_1$ ,  $q_2$ , and  $q_3$  are particularly designed to be constant, decaying, and growing states, respectively, and the corresponding characteristic frequency increases with  $n$  ([Table 1](#)).

**Table 1**  
Constants for the fabricated pattern.

$n$	$a_n$	$b_n$	$\beta_n$	$\gamma_n$	$f$ (Hz)	$\alpha_n(t)$
<b>1</b>	0.030	0.050	0.8	0.8	0.5	1
<b>2</b>	0.015	0.035	0.55	1.8	1.64	$e^{-t/30} - 0.1$
<b>3</b>	0.0075	0.020	0.3	2.4	4.0	$1 - e^{-t/20} + 0.2$

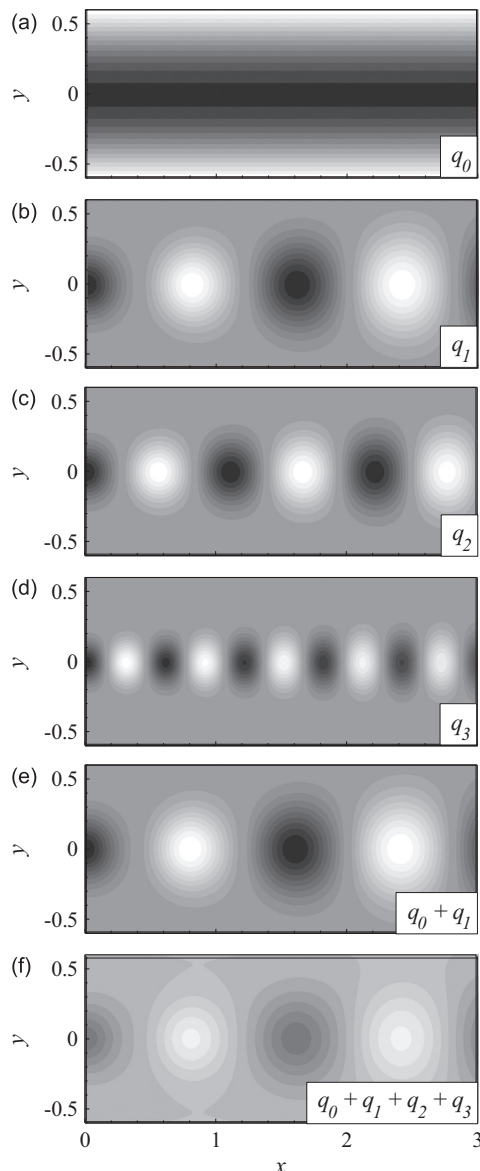


**Fig. 1.** Fabricated patterns.

Here, the multi-dominant structure pattern is constructed by superimposing the three structures of different sizes and frequencies onto the stationary field, as shown in Fig. 1f. A total of 2000 successive snapshots with a sampling frequency of 100 Hz were analyzed using the POD algorithm, and the eigenvalue of each mode and its cumulative distribution are shown in Fig. 2. As the mode number increases, the eigenvalue is rapidly reduced for the first six eigenmodes, and then collapses sharply to an negligible level. Correspondingly, the cumulative energy of the first six modes reaches 99.7% of the total, and the convergence speed considerably slows down as more eigenmodes are included. As seen in Fig. 2, the first two modes contain most of the fluctuation energy, reaching 35.3% and 32%, respectively. The fluctuation energies of the third and fourth modes are rapidly reduced to 11% and 9.5%, respectively and those of the fifth and sixth modes are both around 5.8%. Thus, the first six modes would give an accurate reflection of the three buried structures.

The spatial distributions of the first six POD modes are shown in Fig. 3, a general view of which shows that the first, second, and third pairs of POD modes share similarities with the structures  $q_1$ ,  $q_2$ , and  $q_3$  shown in Fig. 1, respectively. A spatial correlation with the streamwise shift of  $\lambda/4$  is also established between each pair of the POD modes. This indicates that the first, second, and third pairs of the POD modes would generally represent the structures  $q_1$ ,  $q_2$ , and  $q_3$ , respectively. However, a comparative view of Figs. 1 and 3 discloses significant distortions in the structures marked by white arrows (Fig. 3). These are attributed to the contamination of the desired mode by the other two uncorrelated structures, which will be revisited in Fig. 6.

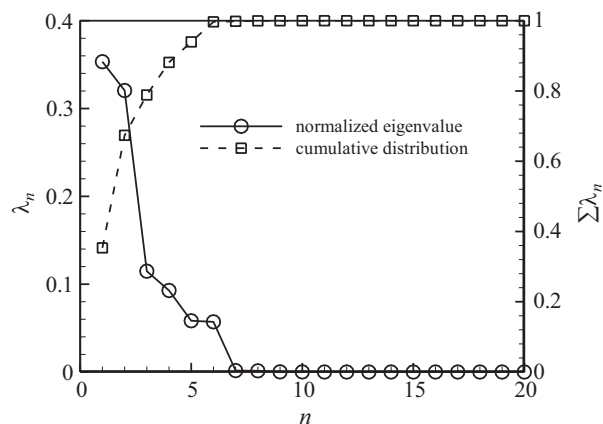


**Fig. 2.** Normalized eigenvalue and its cumulative distribution of POD modes extracted from the fabricated multi-dominant structure pattern.

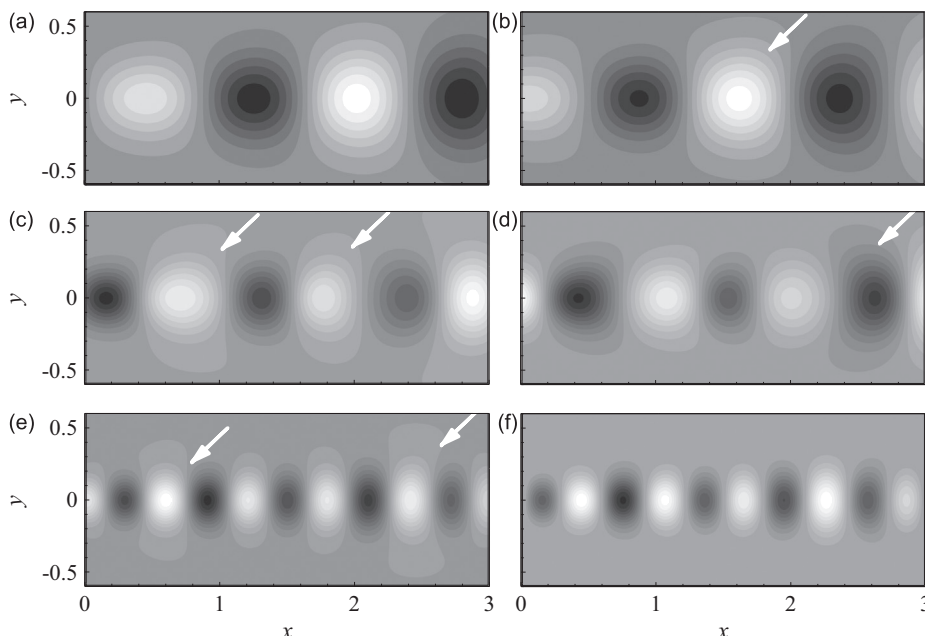


**Fig. 3.** The first six POD modes extracted from the fabricated multi-dominant structure pattern.

The temporal DMD analysis performed on snapshots of the multi-dominant structure pattern determined the Ritz values, DMD spectrum, and energy spectra of all of the DMD modes, which are plotted in Fig. 4. The extracted Ritz values  $\lambda_j$  of the matrix  $C$  shown in Fig. 4a tend to be well distributed on the unit circle in the complex plane of  $|\lambda_j| = 1$ , identifying the existence of three distinct structures. The logarithmic mapping of the Ritz values in Fig. 4b determines that the structure  $q_1$  marked by 1 remains constant while the structures  $q_2$  marked by 2 and  $q_3$  marked by 3 are in the stable (decaying) and unstable (growing) states, respectively. In Fig. 4c, four distinct amplitude peaks marked by 0, 1, 2, and 3 with the corresponding frequencies of 0, 0.5, 1.64, and 4.0 Hz, respectively, are readily picked up from the extracted spectra based on the global energy norm of each mode. Subsequently, the spatial distributions of the real and imaginary parts of each DMD mode are shown in Fig. 5. Clearly, the first, second, and third DMD modes are generally in good conformity with the structures  $q_1$ ,  $q_2$ , and  $q_3$  as shown in Fig. 1, respectively. The above-mentioned information determined from the temporal DMD analysis agrees well with the predefined facts about the fabricated pattern (Table 1), i.e., frequency, growth/decay rate, and spatial features. Thus, the first, second, and third temporal DMD modes could give a full representation of the structures  $q_1$ ,  $q_2$ , and  $q_3$ , respectively. Recall that there are obvious discrepancies between the spatial features of the POD modes shown in Fig. 3 and the original structures shown in Fig. 1, whereas no such discrepancies are found for the temporal DMD modes. This remarkable difference results from the fundamental concerns of the POD and DMD algorithms. Using the second-order statistics as a basis for decomposition, the POD algorithm carries out the eigenvalues decomposition to produce a hierarchy of coherent structures based on the time-averaged spatial correlation tensor. However, the temporal DMD algorithm extracts the dominant features from the snapshot sequences by approximating the linear mapping between the snapshots. Schmid (2010) concluded that the POD algorithm focuses on a representation based on the spatial orthogonality, whereas both the temporal orthogonality (frequencies) and the spatial orthogonality are considered by the temporal DMD algorithm.

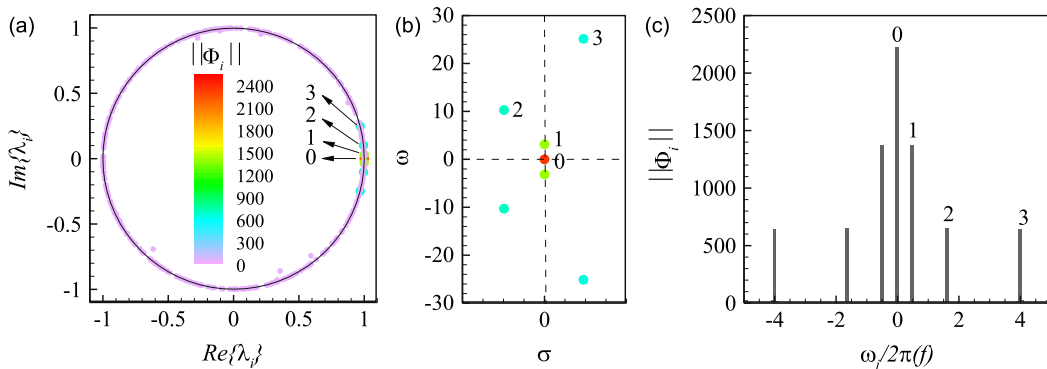


**Fig. 4.** Ritz values (a), DMD spectra (b), and energy spectra (c) of temporal DMD modes extracted from the fabricated multi-dominant structure pattern.

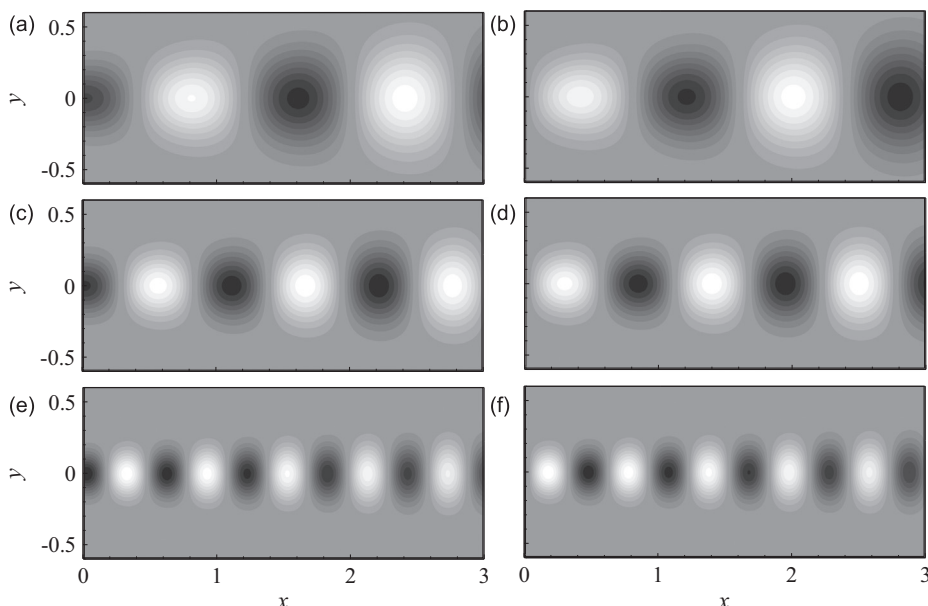


**Fig. 5.** Real part (a, c, e) and imaginary part (b, d, f) of temporal DMD modes extracted from the fabricated multi-dominant structure pattern.

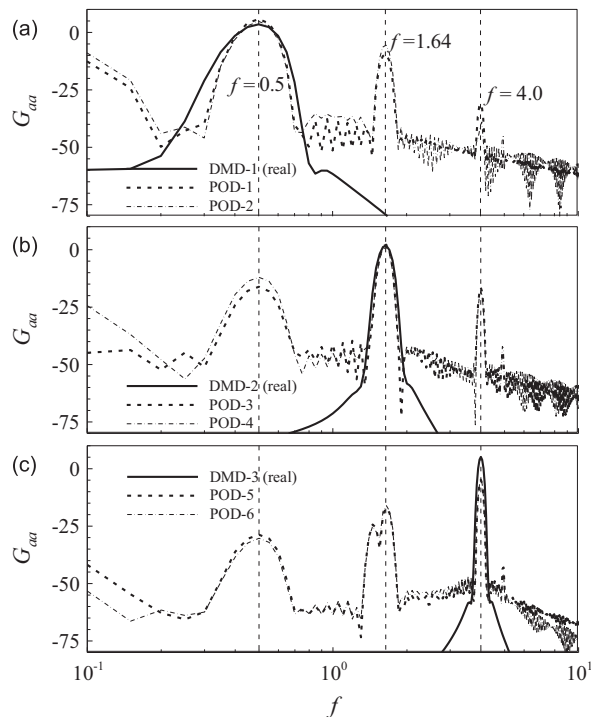


**Fig. 6.** Power spectra of temporal DMD and POD mode coefficients extracted from the fabricated multi-dominant structure pattern.

The leakage of spectral information can be obviously obtained by plotting the power spectra of the POD and temporal DMD coefficients, which are shown in Fig. 6. In Fig. 6a, only one peak at  $f=0.5$  Hz is detected for the first temporal DMD coefficient while three peaked frequencies at  $f=0.5$  Hz, 1.64 Hz, and 4.0 Hz are obvious for the first pair of POD coefficients. The defects of this so-called frequency leakage are also found in the second and third pairs of POD coefficients (Fig. 6b and c) while the second and third temporal DMD mode coefficients are overwhelmingly peaked at  $f=1.64$  Hz and 4.0 Hz, respectively. Accordingly, compared to the POD algorithm, the well-captured spatial pattern shown in Fig. 5 and the spectra shown in Fig. 6 demonstrate that the first, second, and third temporal DMD modes can cleanly separate the fabricated structures  $q_1$ ,  $q_2$ , and  $q_3$ , respectively. Again, this is closely associated with the temporal (spectral) and spatial orthogonalities featured in the temporal DMD algorithm. However, for the multi-dominant structure pattern, although the general patterns of the first, second, and third pairs of the POD modes match the corresponding predefined structures, the POD algorithm fails to cleanly and separately extract the desired dominant structures, which are unfortunately contaminated by the other uncorrelated structures.

Subsequently, the spatial DMD analysis was applied to the multi-dominant structure pattern and the energy spectrum and corresponding modes were plotted in Fig. 7. In Fig. 7a, there are distinct peaks near three wavelengths:  $\lambda_x = 1.63$ ,  $\lambda_x = 1.12$  and,  $\lambda_x = 0.59$ , of which the corresponding modes are shown in Fig. 7b–d. Examining the contour variations in the dominant structures along the time axis discloses that the growth status of the three modes are zero, decay, and grow, respectively while their convection speeds were 0.81, 1.83, and 2.36, respectively. This information closely matches the predefined parameters of  $q_1$ ,  $q_2$ , and  $q_3$  listed in Table 1. In Fig. 7a, the existence of the scattered peaks near  $\lambda_x = 1.12$  and  $\lambda_x = 0.59$  is resulted from different sampling time, which can also be interpreted as number of snapshots. For small sampling time only one mode is resolved around the peak, while for the higher sampling time, more than one modes can be detected (Muld et al., 2012).

#### 4.2. Case study of real flow behind a single cylinder

Here, the case study of the wake behind a single cylinder at high Reynolds number is used for the comparative study, in which several high-order harmonics are superimposed with the dominant Karman-like vortex street in the disturbance field. The experimental measurements were carried out in a closed-loop recirculating water channel previously used by Shi et al. (2013). The cross-sectional size of the test section is  $100 \times 100$  mm<sup>2</sup> and a single cylinder of diameter  $D=8$  mm, spanning the entire width of the test-section, is placed in the water channel at the middle depth. Fig. 8 shows a schematic diagram of the measurement regions. The free stream velocity was kept at  $U_0=1.0$  m/s, resulting in a Reynolds number based on the diameter of the cylinder  $Re_D=8000$ . The free-stream turbulence intensity is less than 2%. The wake behind the single cylinder was measured using the planar TR-PIV. Glass beads ( $\rho \approx 1.05$  kg/m<sup>3</sup>,  $d \approx 10$   $\mu$ m) were used as tracer particles

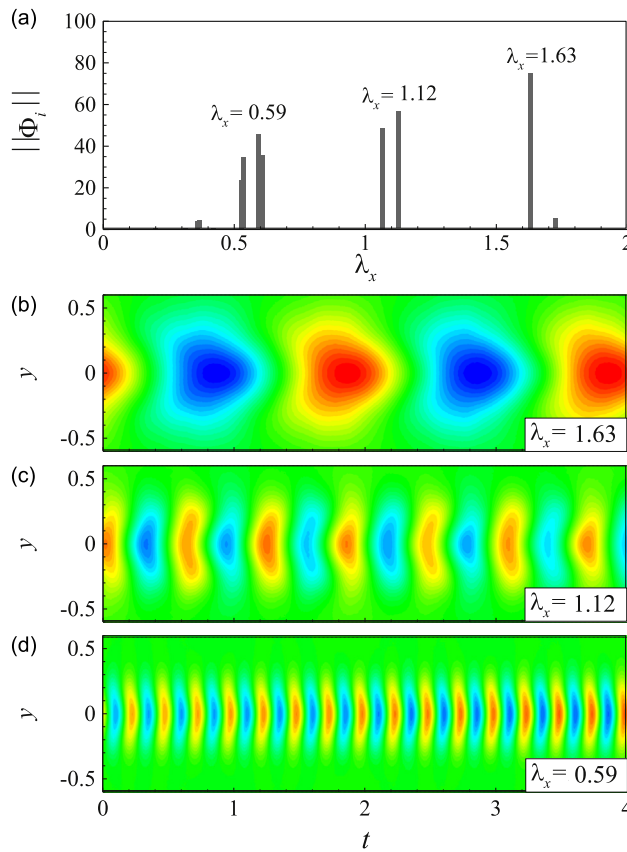


**Fig. 7.** Energy spectrum (a) and corresponding DMD modes (b-d) extracted from the single-dominant structure pattern using spatial DMD analysis.

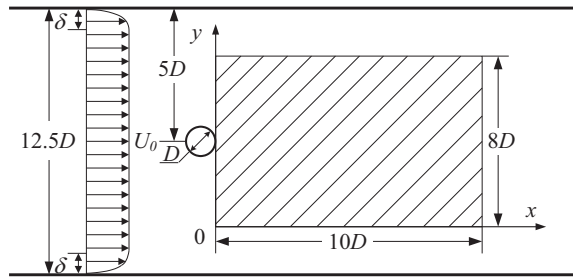


**Fig. 8.** Schematic diagram of the experimental setup: wake flow behind a single cylinder.

and the middle plane was illuminated by an 8 W continuous-wave semiconductor laser (532 nm). The appropriate combination of cylindrical lenses was fitted to the compact laser to produce a 1 mm-thick light sheet behind the cylinder. A high-speed camera (SpeedSense, Dantec) was used to acquire the seeded images. In experiment, the camera was operated at  $1280 \times 800$  pixels with a framing rate of 1400 Hz, which is sufficient to cover the range of frequencies of interest. Here, a total of 10 000 images of the seeded flow were successively acquired. The standard cross-correlation PIV algorithm, in combination with window offset, sub-pixel recognition by Gaussian fitting, and sub-region distortion, were used to determine the velocity fields. The test region was chosen as  $10D \times 8D$  to cover the range of flow field of interest. The interrogation window size was  $32 \times 32$  pixels with a 50% overlap, which yielded a measurement grid of velocity vectors with a spacing of  $1.28 \times 1.28$  mm $^2$ . The error in measuring the particle displacement between two images was less than 0.1 pixels, and the uncertainty in the measurement of the velocity field was less than 2%.

The POD analysis was performed to the 10 000 snapshots of the wake flow. The normalized eigenvalues and cumulative distributions of POD modes are shown in Fig. 9, which reveals that the eigenvalues are reduced rapidly beyond the first two eigenmodes. The first two POD modes contain more than 56.6% of the fluctuation energy. As the mode number  $n$  increase, the eigenvalues continue to reduce and remain at very low magnitudes. By checking the spatial distribution of the POD modes shown in Fig. 10, in which the contour plot represents the longitudinal velocity fluctuation, it is obviously that the

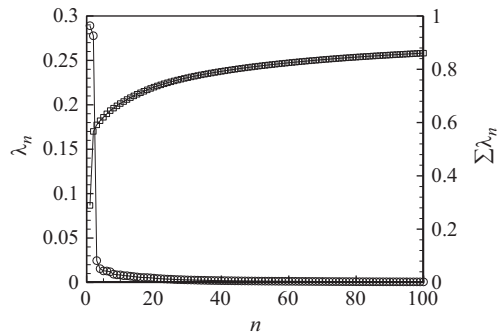


**Fig. 9.** Normalized eigenvalues and cumulative distributions of POD modes.

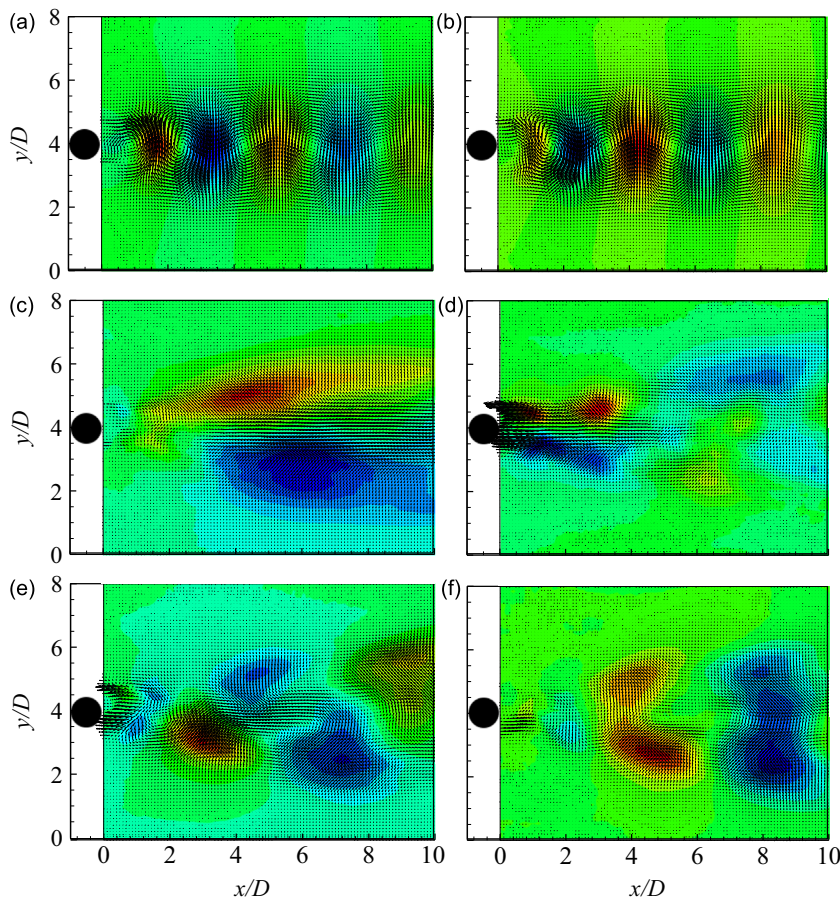


**Fig. 10.** The first six POD modes extracted from the wake of the single cylinder.

first two POD modes correspond to the Karman-vortex street. However, for the next four POD modes shown in Fig. 10c-f, it is much difficult to determine the physical significance of the structures with larger extents in both streamwise and longitudinal directions.

Next, the temporal DMD analysis was employed to describe the wake flow behind the single cylinder; the Ritz values and energy spectra of all DMD modes are plotted in Fig. 11. Similar to the multi-dominant structure of fabricated pattern, the extracted Ritz values  $\lambda_j$  of the matrix  $C$  shown in Fig. 11a tend to be well distributed on the unit circle in the complex plane of  $|\lambda_j| = 1$ , identifying the existence of three distinct structures. In Fig. 11b, four distinct amplitude peaks marked by 0, 1, 2, and 3 with the corresponding frequencies of 0, 25.6, 50.4, and 76.9 Hz, respectively, are readily picked up from the extracted spectra based on the global energy norm of each mode, which are summarized in Table 2. Here, the frequencies 50.4 and 76.9 Hz are approximately the integral multiple of the basic frequency of 25.6 Hz, corresponding to the high-order harmonics in the disturbance field.

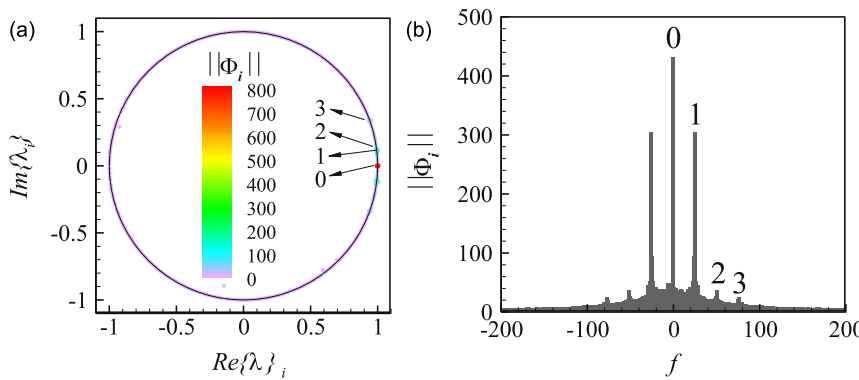


**Fig. 11.** Ritz values (a) and energy spectra (b) of temporal DMD modes.

**Table 2**  
Frequency, wavelength and convection speed of the three dominant dynamic modes.

	Mode 1	Mode 2	Mode 3
$f$ (Hz)	25.6	50.4	76.9
$\lambda_x$ (mm)	33.04	17.2	11.54
$c/U_\infty$	0.85	0.87	0.88

Subsequently, the spatial distributions of the real part of each DMD mode are shown in Fig. 12, in which the longitudinal component of the corresponding mode is contour plotted for ease of understanding. Obviously, the first DMD mode is assigned to be the Karman-vortex street; the streamwise wavelength  $\lambda_x$  can be estimated by measuring the streamwise distance of two neighboring structures, as illustrated in Fig. 12a. The dominant dynamic modes at frequencies of 25.6, 50.4 and 76.9 Hz are corresponding to three periodically convecting vortices in hierarchy of descending scale, e.g. higher-order harmonics take along finer-scale structures. In addition, a general view of Fig. 12 shows that the small-scale structures expand faster than the large-scale ones along the longitudinal direction. The frequency, wavelength and convection speed of these three DMD modes are summarized in Table 2.

#### 4.3. Case study of real flow behind two cylinders of different size

The subsequent case study of the wake behind two side-by-side cylinders of different diameters was performed to provide a comparative view of the extracted structures using the POD and DMD analysis. The experimental measurements of the complex wake were carried out in a recirculation open water channel. The cross-sectional size of the water channel is  $150 \times 250 \text{ mm}^2$ . Detailed information regarding the water channel is referred to Liu et al. (2011a). Fig. 13 provides a schematic diagram of the measurement regions where two circular cylinders of different sizes ( $D=8 \text{ mm}$ ), spanning the entire width of the test-section, are placed side-by-side in the water channel at the middle depth. Two cases with different vertical gaps between the side-by-side cylinders were studied, i.e.,  $G/D=0.5$  and 2.0. The aspect ratio of the experimental model was considered large enough to ensure a statistically two-dimensional flow in the central plane of the wake based on the suggestion of Brederode (1978). The free-stream velocity was maintained at 0.125 m/s, which results in a Reynolds number of  $\text{Re}_D=1000$  based on the diameter of the small cylinder. The free-stream turbulence intensity is less than 2%. The sidewalls of the water channel are made of Plexiglas for easy optical access in PIV measurements.

The wake behind the two side-by-side cylinders of different sizes was measured using the planar TR-PIV. Glass beads ( $\rho \approx 1.05 \text{ kg/m}^3$ ,  $d \approx 10 \mu\text{m}$ ) were used as tracer particles and the middle plane was illuminated by an 8 W continuous-wave semiconductor laser (532 nm). A high-speed CMOS camera (Mikrotron, American) was used to acquire the seeded images and image distortion was suppressed using a 200 mm lens (PC Micro Nikon, Japan). The appropriate combination of cylindrical lenses was fitted to the compact laser to produce a 1 mm-thick light sheet behind the cylinder. The CMOS camera used in the experiment has a typical  $1280 \times 1024$  pixels with a full framing rate of 500 Hz. In this study, the camera was operated at  $1280 \times 1024$  pixels with a framing rate of 250 Hz, which is sufficient to cover the range of frequencies of interest. As Fig. 13 reveals, two adjacent regions ( $9.0D \times 7.2D$ ), separated by  $0.3D$  in the streamwise direction, were separately measured by traversing the light sheet and the camera. During the experiment, a RAID system of 16 SSDs at a total of storage of 1TB, in combination with two full Camera-link interfaces between the high-speed camera and the image adapter card, facilitates the real-time data transfer from the camera to the disks. Here, a total of 10 000 images of the seeded flow were successively acquired. The interrogation window size was  $32 \times 32$  pixels with a 50% overlap, which yielded a measurement grid of velocity vectors with a spacing of  $0.9 \times 0.9 \text{ mm}^2$ .

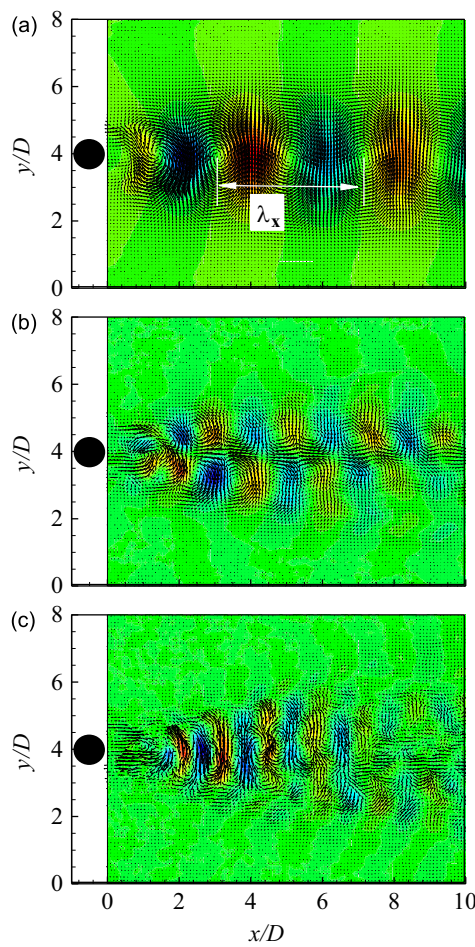


**Fig. 12.** DMD modes extracted from the wake of the single cylinder.

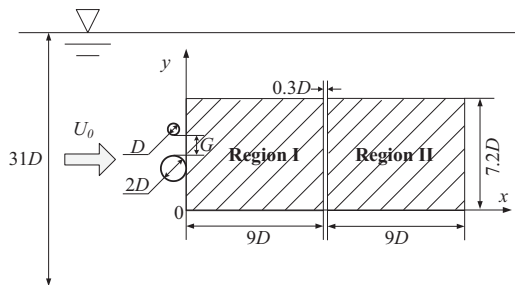


**Fig. 13.** Schematic diagram of the experimental setup: wake flow behind two cylinders of different diameter.

Before viewing the extracted structures using the POD and DMD algorithms, a preliminary view of the time-mean and instantaneous wakes at the different gap widths between the two cylinders is recorded in Fig. 14. In conformity with the findings of [Mahbub Alam et al. \(2003\)](#), the general pattern of the wakes at  $G/D=0.5$  and 2.0 exhibit entirely different characteristics. For  $G/D=0.5$ , a low-speed jet flow is issued along the small gap, as shown in Fig. 14a, with the two cylinders acting as an apparent 'single' cylinder of larger diameter so that a very large low-speed recirculation zone is formed in the near wake of the cylinders. In the far wake region the pattern is generally featured as that behind a single larger cylinder. In Fig. 14b, a single Karmen-like vortex street is formed in the bulk region of the cylinders. For  $G/D=2.0$ , the energetic flow issuing from the large gap interacts with the top and bottom shear layers, giving rise to two wake patterns without obvious interaction in the near wake region, as shown in Fig. 14c. As the fluid flows downstream, the continuous entrainment of the fluid into the top and bottom vortical structures results in a considerable reduction in the flow velocity at the central region.

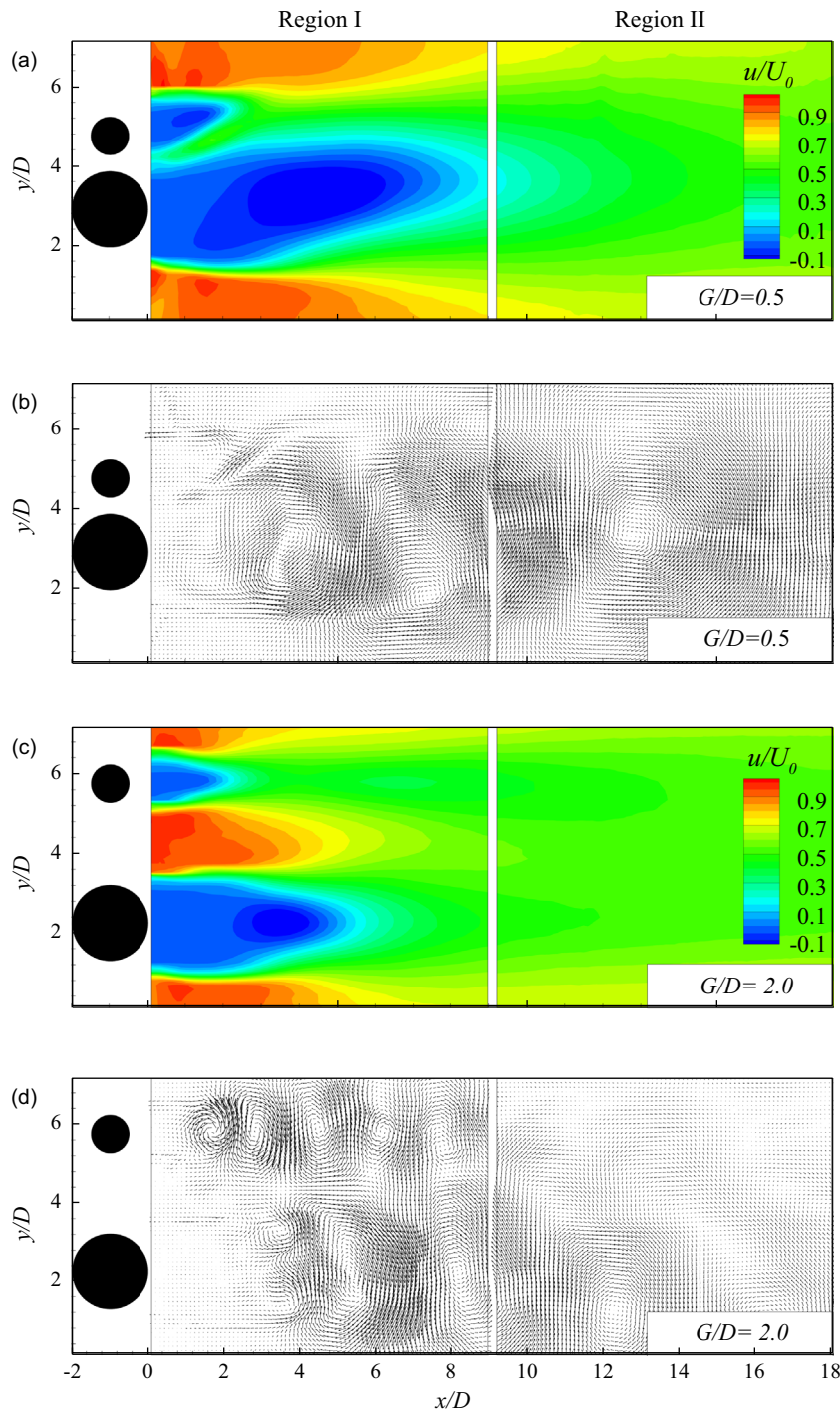


**Fig. 14.** Distributions of time-mean streamwise velocity (a, c) and an instance of the instantaneous fluctuation velocity vectors (b, d).

Correspondingly, beyond the station  $x/D=10$ , the top small structures with low fluctuation energy quickly decay while the bottom large structures with large fluctuation energy continue to evolve downstream (Fig. 14d).

The POD analysis were made separately based on the 10 000 snapshots of two regions, and the eigenvalues and corresponding modes for the case  $G/D=0.5$  are shown in Fig. 15, which reveals that the eigenvalues are reduced rapidly beyond the first two eigenmodes for two regions: I and II. The amplitudes of the first two eigenvalues corresponding to the flow in region I are much lower than those in region II. The sharp change is due to the dominant role of the large vortical structure in region II (Fig. 15b and c) while in region I the limited recirculation zone behind the top small cylinder reduces

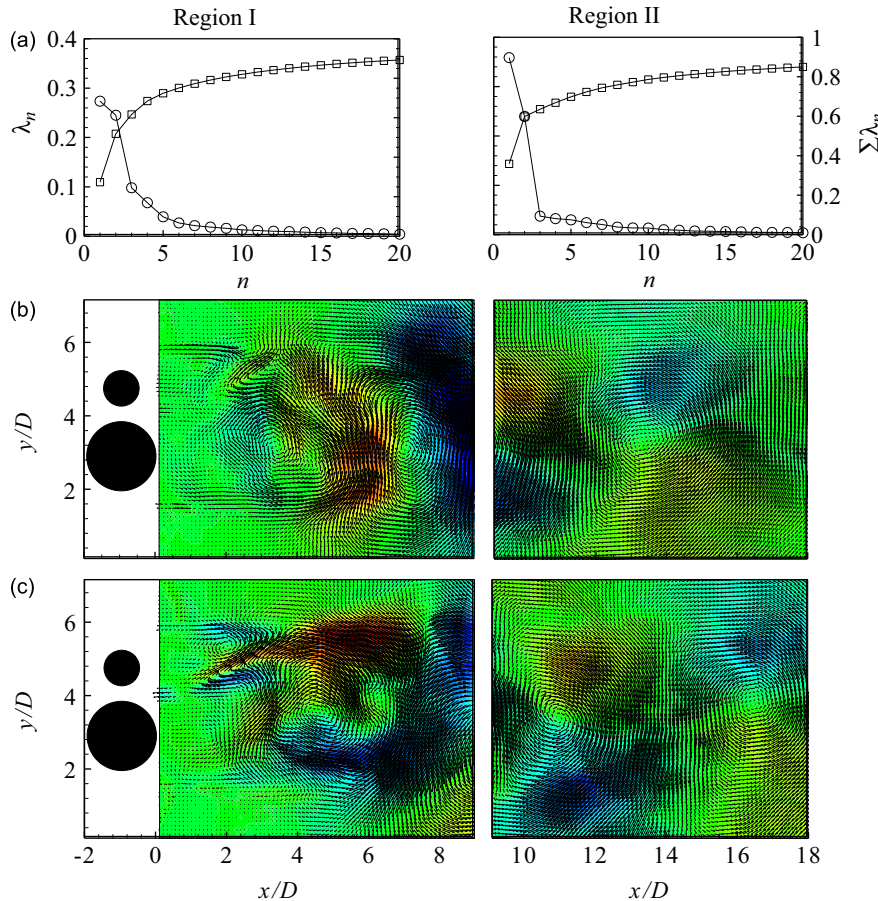


**Fig. 15.** Normalized eigenvalues, cumulative distributions (a) and spatial patterns (b, c) of POD modes for case  $G/D=0.5$ .

the overall energy of the developing vortical structures behind the apparent ‘single’ cylinder. The overall spatial distributions of the first and second POD modes in both regions I and II are similar to the Karman-like vortex street pattern; the distortion of the forming structure by the small recirculation zone is seen in region I (Fig. 15b and c).

In regions I and II for case  $G/D=0.5$ , the energy spectra and the decomposed modes using the temporal DMD algorithm are shown in Fig. 16. The dominant frequency of the first DMD mode is detected at  $f=1.0$  Hz, meaning that the dynamically evolving structures are evolving and dominant in both regions. Likewise, the well-organized structures can be readily recognized from the spatial distributions of the first DMD mode in both regions. Subsequently, the spatial DMD analysis was applied to the velocity fields in both regions and the energy spectrum and corresponding modes are plotted in Fig. 17. Two major peaks,  $\lambda_x/D = 9.9$  and  $11.9$ , are found in regions I and II, respectively. The corresponding modes in both regions relate to a Karman-like vortex street in terms of the frequency information, which is determined to be around 1.0 Hz from the time-dependent variation of the spatial DMD modes in the two regions (Fig. 16). Likewise, the convection speeds of the structures in regions I and II are determined to be  $0.63U_0$  and  $0.76U_0$ , respectively, indicating an increase in the convection speed of the vortical structures as the wake defect is recovered downstream.

As for the case  $G/D=2.0$ , the eigenvalues and the corresponding POD modes are shown in Fig. 18. In region I, the eigenvalues of the first four eigenmodes are much larger than those of the remaining modes, and a sharp reduction is observed with the further increase of the mode number (Fig. 18a). This results from the existence of dual-dominant structures in region I. However, in region II (Fig. 18a), the amplitudes of the eigenvalues are very high for the first two modes, at which point they collapse to a much lower level at the third mode due to the dominance of the bottom large structure in region II, as noted in Fig. 14. A general view of the spatial distributions of the first four POD modes shows that in region I (Fig. 18b-d), the first and second pairs of POD modes generally capture the bottom large and top small vortical structures, respectively. However, close examination of Fig. 18b-d in region I clearly shows the buried footprints of the top small vortical structures in the first pair of POD modes, while those of the bottom large vortical structures are also obviously discernible in the second pair of POD modes. This is attributed to the frequency leakage problem of the POD algorithm, which is associated with the multi-dominant structure pattern (Fig. 6). In the time-averaging process, to obtain the spatial correlation tensor of the POD algorithm, a series of uncorrelated flow structures are involved. In region II, the first pair of POD modes provide a well-organized representation of the dominant large vortical structures, whereas the second pair of POD modes show the random pattern beyond  $x/D=10$ .

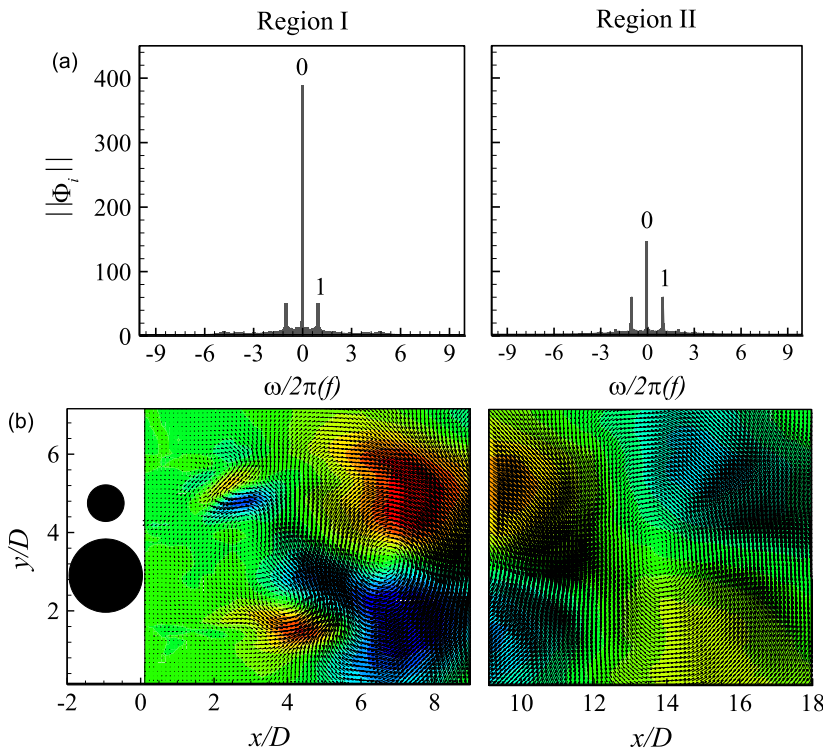


**Fig. 16.** Energy spectra (a) and spatial patterns (b) of temporal DMD modes for case  $G/D=0.5$ .

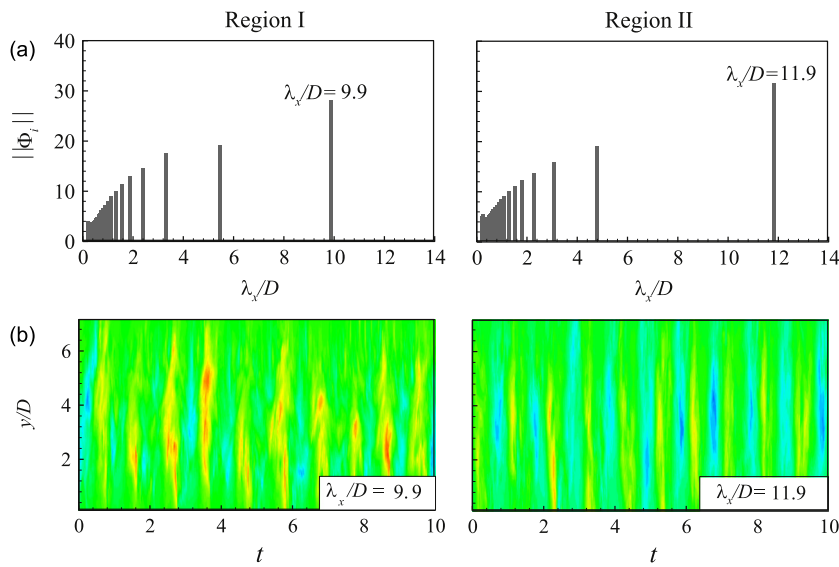


**Fig. 17.** Energy spectra (a) and corresponding DMD modes (b) for case  $G/D=0.5$  using spatial DMD analysis.

By performing the temporal DMD analysis of the sampled snapshots in both regions I and II, we determined the energy spectrum and the corresponding temporal DMD modes, which are shown in Fig. 19. The existence of the first and second DMD modes is obviously picked up in region I (Fig. 19a), whereas only the first DMD mode can be found in region II (Fig. 19a). In region I, the first DMD mode has the unique features of the bottom large structures shedding from the large cylinder while the top small structure shedding from the small cylinder is clearly seen in the second DMD mode. A close examination of the spatial distributions of these two DMD modes in Fig. 19 in region I does not reveal any discernible signatures of the other uncorrelated structures, confirming that the temporal DMD analysis cleanly separated the contributions of two uncorrelated dominant structures. In region II, the large structures are obviously located in the

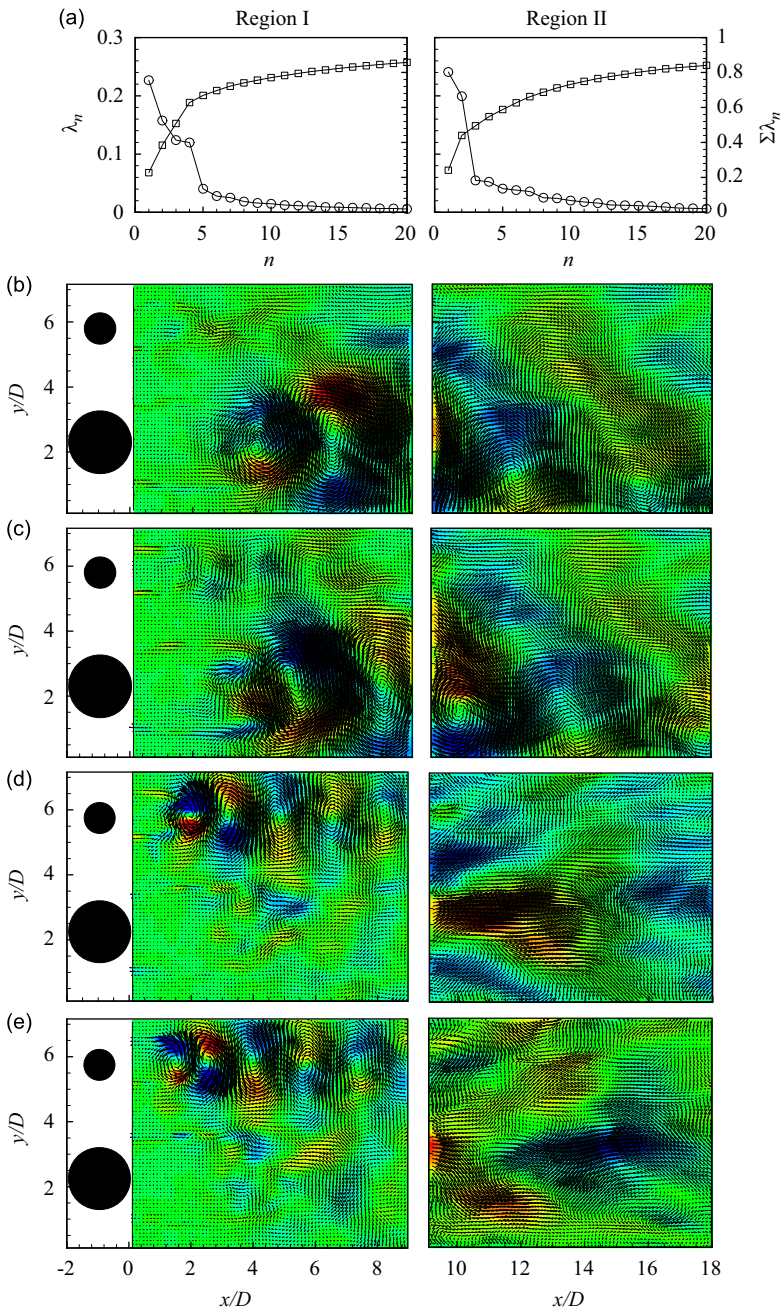


**Fig. 18.** Normalized eigenvalues, cumulative distributions (a) and spatial patterns (b–e) of POD modes for case  $G/D=2.0$ .

bottom area behind the large cylinder while no traces of small structures are seen in the top area behind the small cylinder. This is consistent to the observation in Fig. 14d in region II.

Subsequently, the spatial DMD analysis was applied to the velocity fields in both regions with the energy spectrum and corresponding modes plotted in Fig. 20. Two major peaks,  $\lambda_x/D = 5.8$  and 3.3, are detected in region I. The peak in the wavelength  $\lambda_x/D = 5.8$  corresponds to the Karman vortex street behind the bottom larger cylinder, which is seen from the time-dependent variation of the first DMD mode. In the second DMD mode, the intensified signatures along  $y/D = 6.5$  result from the Karman vortex street ( $\lambda_x/D = 3.3$ ) behind the top smaller cylinder; however, the signatures of the Karman vortex street behind the bottom larger cylinder ( $\lambda_x/D = 5.8$ ) are not excluded as expected, which is attributed to a defect in wavelength leakage. In region II, the major peak near  $\lambda_x/D = 8.8$  corresponds to the Karman vortex street behind the bottom larger cylinder. The large increase in the peaked primary wavelength from region I to region II indicates the intensified convection speed of the vortical structures from

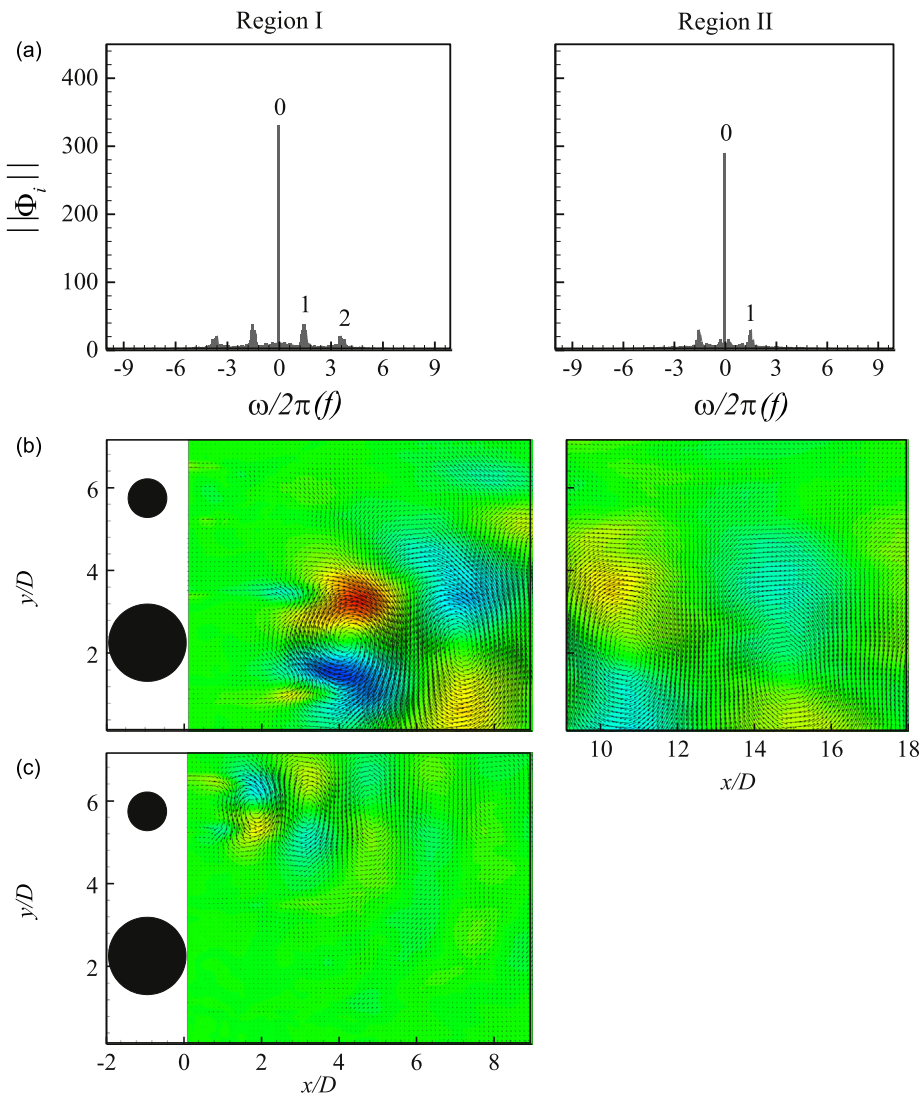


**Fig. 19.** Energy spectra (a) and spatial patterns (b, c) of temporal DMD modes for case  $G/D=2.0$ .

0.67 $U_0$  to 0.84 $U_0$ . However, a comparative view of Fig. 20 in both region I and II discloses the reduced energy of the decaying vortical structures behind both the top and bottom cylinders as the fluid flows downstream from region I.

## 5. Conclusions

In the present study, we conducted a comprehensive comparison of the ability of the POD and DMD algorithms to extract multi-dominant coherent structures superimposed in fluid flows. The influences that multi-dominant structures and high-order harmonics had on the decomposed modes were taken into extensive consideration. A series of fabricated patterns was firstly constructed for the benchmark testing to simulate multi-dominant convective structures superimposed in a stationary field; three structures were built with different spectral and spatial features for ease of comparison. The comparison showed that the temporal DMD method could clearly separate each structure in the spatial and spectral senses. However, an examination of the POD modes and the spectrum curves of each POD coefficient convincingly demonstrated that the POD mode corresponding to the desired structure is contaminated by the other uncorrelated structures. Subsequently, two case studies of the real wake flows, which were determined from high-repetition TR-PIV measurements, were employed to demonstrate the discrepancies of the POD and DMD algorithms in extracting the multi-dominant coherent structures. For the wake flow behind a single cylinder at  $Re_D=8000$ , the first two POD modes are related to the Karman-like vortex street; for the higher-order POD modes, it is much difficult to determine the physical significance of the structures with larger extents in both streamwise and longitudinal directions. Whereas, the temporal DMD algorithm accurately determined the frequency, wavelength and convection speed of the Karman-like vortex street and its higher-

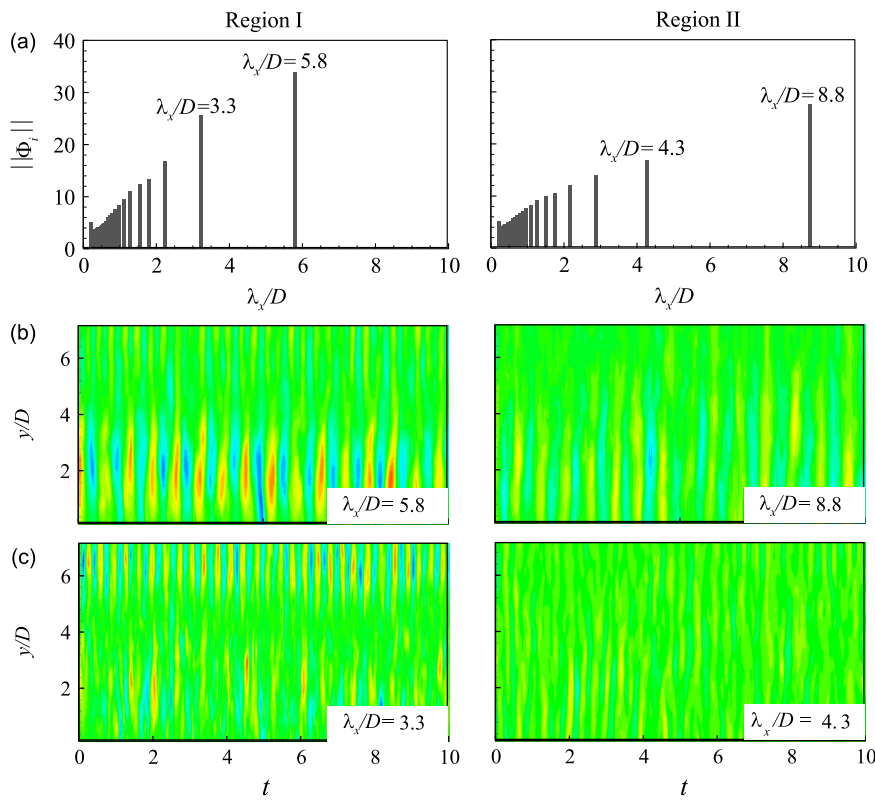


**Fig. 20.** Energy spectra (a) and corresponding DMD modes (b, c) for case  $G/D=2.0$  using spatial DMD analysis.

order harmonics. Finally, the wake flow behind two side-by-side cylinders of different diameters were measured, resulting in time-series wake instances superimposed with a single-dominant convective structure ( $G/D=0.5$ ) or dual-dominant convective structures ( $G/D=2.0$ ). A close inspection of the decomposed modes revealed that the first temporal DMD mode and the first pair of POD modes could effectively capture the major features of the single-dominant structure at  $G/D=0.5$ . For the wake flow at  $G/D=2.0$ , the first and second temporal DMD modes effectively and independently extracted the Karman-like vortex structures behind the large and small cylinders, respectively. Meanwhile, although the first and second pairs of POD modes generally captured these two convecting structures, respectively, there was obvious existence of the undesirable contamination of the POD mode, as reflected in the interaction between the desired and uncorrelated structures. Of noted is that the temporal DMD algorithm works well with the time-resolved data in extracting the temporally and spatially varying coherent structures, which is however not valid when the data sets are obtained with much low sampling rate. In addition, the present DMD algorithm is still limited to the instances sampled at constant time interval. However, the POD algorithm could work for the randomly sampled realizations without limitation of the sample rate.

## Acknowledgment

The authors gratefully acknowledge financial support from the National Natural Science Foundation of China (Grant nos. 51176108 and 11372189) for this study.

## References

- Bagheri, S., 2010. Analysis and Control of Transitional Shear Flows Using Global Modes. Linkoping.
- Bisset, D., Antonia, R., Browne, L., 1990. Spatial organization of large structures in the turbulent far wake of a cylinder. *Journal of Fluid Mechanics* 218, 439–461.
- Brederode, D., 1978. Influence of the side walls on the turbulent center-plane boundary-layer in a square duct. *ASME, Transactions, Journal of Fluids Engineering* 100, 91–96.
- Chen, W.Y.C., Louck, J.D., 1996. The combinatorial power of the companion matrix. *Linear Algebra and its Applications* 232, 261–278.
- Deri, E., Braza, M., Cid, E., Cazin, S., Michaelis, D., Degouet, C., 2013. Investigation of the three-dimensional turbulent near-wake structure past a flat plate by tomographic PIV at high Reynolds number. *Journal of Fluids and Structures* 47, 21–30.
- Gilka, G., Luchtenburg, D.M., Thiele, F., Morzynski, M., 2010. Dynamic characterization of an actuated bluff body wake. In: Proceedings of V European Conference on Computational Fluid Dynamics, ECCOMAS CFD.
- Hayakawa, M., Hussain, F., 1989. Three-dimensionality of organized structures in a plane turbulent wake. *Journal of Fluid Mechanics* 206, 375–404.

- Hunt, J.C., Wray, A., Moin, P., 1988. Eddies, streams, and convergence zones in turbulent flows. *Studying Turbulence Using Numerical Simulation Databases* 2, 193–208.
- Hussain, A., Hayakawa, M., 1987. Eduction of large-scale organized structures in a turbulent plane wake. *Journal of Fluid Mechanics* 180, 193–229.
- Kim, S.M., Yi, S.J., Kim, H.D., Kim, J.W., Kim, K.C., 2010. Dynamic analysis of bubble-driven liquid flows using time-resolved particle image velocimetry and proper orthogonal decomposition techniques. *Journal of Visualization* 13, 213–220.
- Liu, Y.Z., Shi, L.L., Yu, J., 2011a. TR-PIV measurement of the wake behind a grooved cylinder at low Reynolds number. *Journal of Fluids and Structures* 27, 394–407.
- Liu, Y.Z., Shi, L.L., Zhang, Q.S., 2011b. Proper orthogonal decomposition of wall-pressure fluctuations under the constrained wake of a square cylinder. *Experimental Thermal and Fluid Science* 35, 1325–1333.
- Lumley, J.L., 2007. Stochastic Tools in Turbulence. Dover Publications, N.Y., USA.
- Mahbub Alam, M., Moriya, M., Sakamoto, H., 2003. Aerodynamic characteristics of two side-by-side circular cylinders and application of wavelet analysis on the switching phenomenon. *Journal of Fluids and Structures* 18, 325–346.
- Meyer, K.E., Pedersen, J.M., Ozcan, O., 2007. A turbulent jet in crossflow analysed with proper orthogonal decomposition. *Journal of Fluid Mechanics* 583, 199–228.
- Mezić, I., 2005. Spectral properties of dynamical systems, model reduction and decompositions. *Nonlinear Dynamics* 41, 309–325.
- Muld, T.W., Efraimsson, G., Henningson, D.S., 2012. Flow structures around a high-speed train extracted using proper orthogonal decomposition and dynamic mode decomposition. *Computers and Fluids* 57, 87–97.
- Noack, B.R., Afanasiev, K., Morzynski, M., Tadmor, G., Thiele, F., 2003. A hierarchy of low-dimensional models for the transient and post-transient cylinder wake. *Journal of Fluid Mechanics* 497, 335–363.
- Pan, C., Yu, D., Wang, J., 2011. Dynamical mode decomposition of Gurney flap wake flow. *Theoretical and Applied Mechanics Letters* 1, 012002–012005.
- Prothiin, S., Djeridi, H., Billard, J.-Y., 2014. Coherent and turbulent process analysis of the effects of a longitudinal vortex on boundary layer detachment on a NACA0015 foil. *Journal of Fluids and Structures* 47, 2–20.
- Rowley, C.W., Mezić, I., Bagheri, S., Schlatter, P., Henningson, D., 2009. Spectral analysis of nonlinear flows. *Journal of Fluid Mechanics* 641, 115–127.
- Ruhe, A., 1984. Rational Krylov sequence methods for eigenvalue computation. *Linear Algebra and its Applications* 58, 391–405.
- Schmid, P., Sesterhenn, J., 2009. Dynamic mode decomposition of experimental data. In: Proceedings of 8th International Symposium on Particle Image Velocimetry, PIV09-0141, Melbourne, Australia.
- Schmid, P.J., 2010. Dynamic mode decomposition of numerical and experimental data. *Journal of Fluid Mechanics* 656, 5–28.
- Seena, A., Sung, H.J., 2011. Dynamic mode decomposition of turbulent cavity flows for self-sustained oscillations. *International Journal of Heat and Fluid Flow* 32, 1098–1110.
- Shi, S., New, T., Liu, Y., 2013. Flapping dynamics of a low aspect-ratio energy-harvesting membrane immersed in a square cylinder wake. *Experimental Thermal and Fluid Science* 46, 151–161.
- Sirovich, L., 1987. Turbulence and the dynamics of coherent structures. I-Coherent structures. II-Symmetries and transformations. III-Dynamics and scaling. *Quarterly of Applied Mathematics* 45, 561–571.
- Tang, Z.Q., Jiang, N., 2012. Dynamic mode decomposition of hairpin vortices generated by a hemisphere protuberance. *Science China Physics, Mechanics and Astronomy* 55, 118–124.
- Zhou, Y., Antonia, R., 1993. A study of turbulent vortices in the near wake of a cylinder. *Journal of Fluid Mechanics* 253, 643–661.
- Zhou, Y., Antonia, R., 1994. Critical points in a turbulent near wake. *Journal of Fluid Mechanics* 275, 59–82.